

REPORT DOCUMENTATION PAGE				Form Approved OMB No. 0704-0188	
<p>The public reporting burden for this collection of information is estimated to average 1 hour per response, including the time for reviewing instructions, searching existing data sources, gathering and maintaining the data needed, and completing and reviewing the collection of information. Send comments regarding this burden estimate or any other aspect of this collection of information, including suggestions for reducing the burden, to the Department of Defense, Executive Services and Communications Directorate (0704-0188). Respondents should be aware that notwithstanding any other provision of law, no person shall be subject to any penalty for failing to comply with a collection of information if it does not display a currently valid OMB control number.</p> <p><b>PLEASE DO NOT RETURN YOUR FORM TO THE ABOVE ORGANIZATION.</b></p>					
1. REPORT DATE (DD-MM-YYYY) 23-07-2007		2. REPORT TYPE Journal Article		3. DATES COVERED (From - To)	
4. TITLE AND SUBTITLE  Analytical and Observational Studies of Internal Waves in the Yellow Sea			5a. CONTRACT NUMBER  5b. GRANT NUMBER  5c. PROGRAM ELEMENT NUMBER 0602435N		
6. AUTHOR(S) Marvi Teixeira, Alex Warn-Varnas, John Apel, Jim Hawkins			5d. PROJECT NUMBER  5e. TASK NUMBER  5f. WORK UNIT NUMBER 73-6838-A7-5		
7. PERFORMING ORGANIZATION NAME(S) AND ADDRESS(ES) Naval Research Laboratory Oceanography Division Stennis Space Center, MS 39529-5004			8. PERFORMING ORGANIZATION REPORT NUMBER NRL/JA/7320-01-0029		
9. SPONSORING/MONITORING AGENCY NAME(S) AND ADDRESS(ES) Office of Naval Research 800 N. Quincy St. Arlington, VA 22217-5660			10. SPONSOR/MONITOR'S ACRONYM(S) ONR		
			11. SPONSOR/MONITOR'S REPORT NUMBER(S)		
12. DISTRIBUTION/AVAILABILITY STATEMENT Approved for public release, distribution is unlimited.					
<b>20070813136</b>					
13. SUPPLEMENTARY NOTES					
<b>14. ABSTRACT</b> <p>This article presents findings regarding the origination &amp; evolution of a large train of internal solitary waves as observed through Synthetic Aperture Radar (SAR). The internal wave train under study propagates into deeper waters away from the coast &amp; most important appears to be generated at a well defined point along a steep topographic variation. The shallow bottom topography revealed itself in the SAR image &amp; provided the opportunity to determine, with a large level of accuracy, the precise area where an internal bore originated. The bore traveled east &amp; broke up into a train of solitary waves. The packets phase speed, wave amplitude, mixed-layer depth, &amp; density difference for a two-layer structure were remotely estimated based on measurements made from the SAR image, the knowledge of the local bathymetry, historical data &amp; a two-layer model. Farther along the propagation path the internal waves exhibited an extremely large degree of dispersion, which was related to changing stratification conditions in the area. This particularly long train of internal waves consisted of seven packets that traveled for three days along a well-defined direction that are probably a consequence of the seasonal intrusion into the region of the low salinity plume of the Yangtze River. Monitoring changes in the dispersion characteristic of a soliton train from one tidal period to the next could render remote information regarding changing stratification condition in the area.</p>					
<b>15. SUBJECT TERMS</b> Internal wave models, Synthetic Aperture Radar, SAR					
16. SECURITY CLASSIFICATION OF:		17. LIMITATION OF ABSTRACT	18. NUMBER OF PAGES	19a. NAME OF RESPONSIBLE PERSON Alex C. WarnVarnas	
a. REPORT Unclassified	b. ABSTRACT Unclassified	c. THIS PAGE Unclassified	UL 14	19b. TELEPHONE NUMBER (Include area code) 228-688-5223	

## Analytical and Observational Studies of Internal Solitary Waves in the Yellow Sea

Marvi Teixeira<sup>†</sup>, Alex Warn-Varnas<sup>‡</sup>, John Apel<sup>§</sup>, and Jim Hawkins<sup>††</sup>

Polytechnic University of  
Puerto Rico  
PO Box 192017  
San Juan, PR 00919-2017,  
USA

Naval Research Laboratory  
Code 7320  
Stennis Space Center, MS,  
USA

<sup>†</sup>Global Ocean Associates  
PO Box 12131  
Silver Spring, MD 20908,  
USA

<sup>††</sup>Planning Systems  
Incorporated  
Slidell, LA 70458, USA

### ABSTRACT

TEIXEIRA, M.; WARN-VARNAS, A.; APEL, J., and HAWKINS, J. 2006. Analytical and observational studies of internal solitary waves in the Yellow Sea. *Journal of Coastal Research*, 22(6), 1403–1416. West Palm Beach (Florida). ISSN 0749-0208.

This article presents findings regarding the origination and evolution of a large train of internal solitary waves as observed through Synthetic Aperture Radar (SAR). The internal wave train under study propagates into deeper waters away from the coast and, most important, appears to be generated at a well-defined point along a steep topographic variation. The shallow bottom topography revealed itself in the SAR image and provided the opportunity to determine, with a large level of accuracy, the precise area where an internal bore originated. The bore traveled east and broke up into a train of solitary waves. The packet's phase speed, wave amplitude, mixed-layer depth, and density difference for a two-layer structure were remotely estimated based on measurements made from the SAR image, the knowledge of the local bathymetry, historical climatological data, and a two-layer model. Farther along the propagation path the internal waves exhibited an extremely large degree of dispersion, which was related to changing stratification conditions along the travel direction that are probably a consequence of the seasonal intrusion into the region of the low salinity plume of the Yangtze River. Monitoring changes in the dispersion characteristics of a soliton train from one tidal period to the next could, therefore, render remote information regarding changing stratification conditions in the area. This particularly long train of internal waves consisted of seven packets that traveled for three days along a well-defined direction. A new analytical model, termed the Dnoidal model, was used to describe the development of the internal waves with time. The extended life of this phenomenon provided an exceptional opportunity to monitor and model its evolution as well as to assess the effects of dispersion as the solitary internal waves propagated east, away from the China coast.

**ADDITIONAL KEY WORDS:** *Internal wave models, Synthetic Aperture Radar, SAR.*

### INTRODUCTION

A 500-km × 500-km (ScanSAR wide mode) image (Figure 1) was used to monitor the origination, evolution, and dissipation of a large train of internal wave packets propagating seaward off the China coast. The images were acquired August 22, 1998 at 0942 by the Canadian satellite Radarsat 1. Medium resolution images, at 100 m per pixel, and full resolution, at 50 m per pixel, were analyzed. Seven packets of internal bore and internal wave type features were followed. The internal bores were generated beside a conspicuous topographic feature. The internal bores that disintegrated into solitons traveled far into the midsection of the Yellow Sea. Observing that the spacing between the wave packets had a high degree of regularity along a well-defined direction and that the overall shape of the wave front was preserved along the travel path, corroborated the fact that this was actually a train of internal waves originated at the same location. Fur-

thermore, the effects of dispersion were clearly seen as the internal waves traveled away from their generation point.

Unlike previous literature, which mostly describes internal waves propagating inshore (LIU *et al.*, 1998; PORTER and THOMPSON, 1998), the internal wave train under study propagated eastward into deeper waters away from the coast and, most important, appeared to be generated at a well-defined area along the shelf break. The remotely inferred profile of bathymetry, which revealed itself in the SAR image, was consistent with the known local topography. This provided the opportunity to determine within a good degree of accuracy, the precise area where these internal waves originated. The steep shelf profile seen at the onset of the internal wave train was used to initialize a hydrodynamic model that reproduces the internal bore seen close and offshore of the shelf break (WARN-VARNAS *et al.*, 2005). We are reporting here on the results obtained with a newly introduced analytical model (APEL, 2003), which is used in this work to help assess the evolution of internal waves as they traveled east.

The packet's phase speed, wave amplitude, wavelength, and water column properties were studied in relation to measurements contained in the Synthetic Aperture Radar (SAR) image and with the knowledge of the local bathymetry and

DOI:10.2112/04-0339.1 received 27 October 2004; accepted in revision 28 April 2004.

This work was supported by the US Office of Naval Research, the US Naval Research Laboratory program element PE62435N, and the ASEE-NAVY Summer Faculty Research Program.



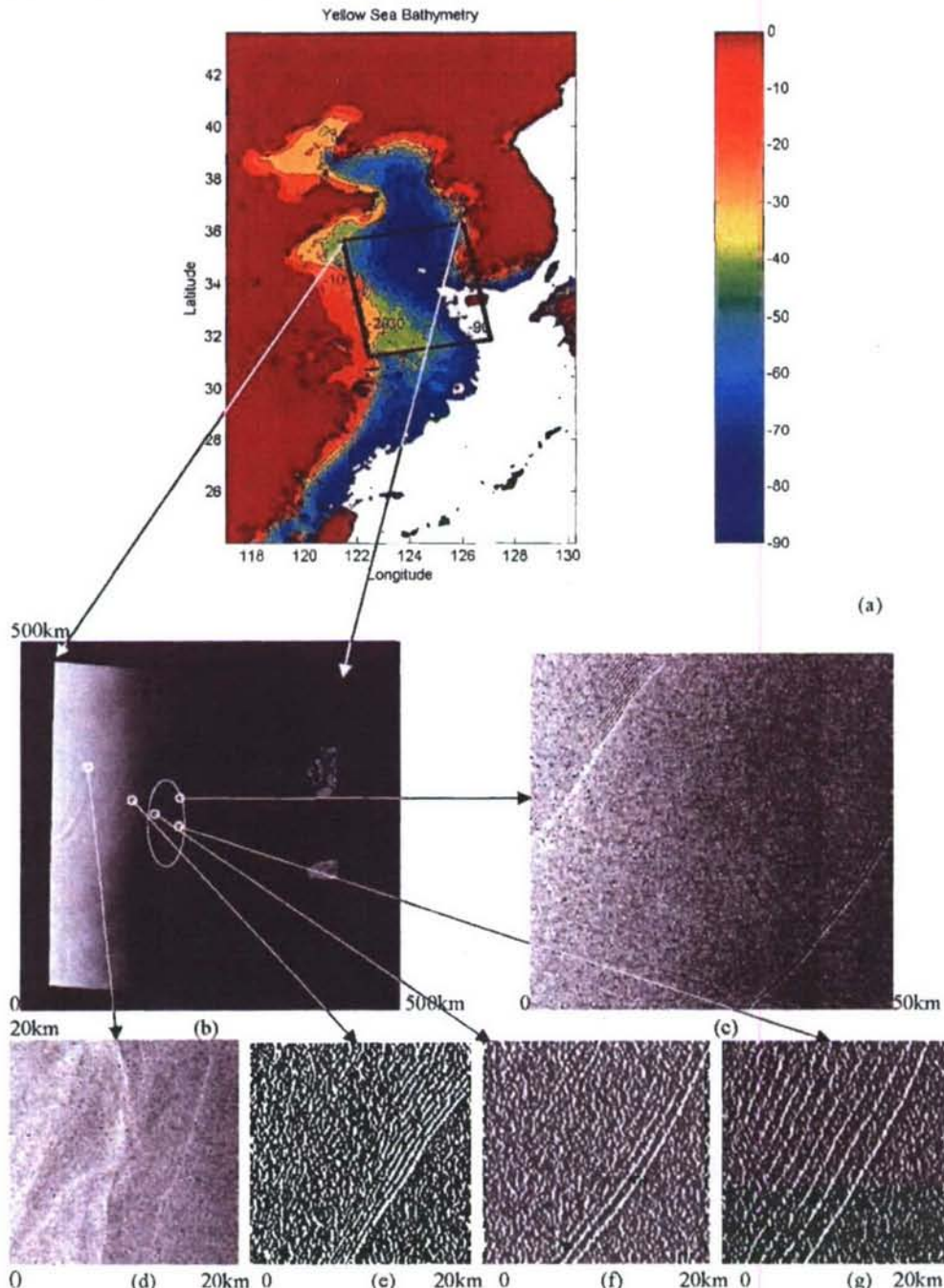


Figure 1. A section of the Yellow Sea, depicting the focus area, as seen in a Radarsat1 ScanSAR (wide) 500 × 500 km image. Pixel spacing is 100 m; August 22, 1998, 0943. The large semicircular pattern seen at the western part of the image (Figure 1b) is a manifestation of the underlying bathymetry. Internal wave packets are formed at this steep topography and travel east. The tip of the Korean peninsula and Cheju Island can be seen at the right. Figures 1d–1g shows the signature of an internal bore as it leaves the shelf break, disintegrates into solitons, and propagates southeast.

historical climatological data. The signature and long life of this event provided a good opportunity to monitor and model its evolution and to assess the effect of dispersion as the internal waves traveled away from the China coast (Figure 1).

The article is organized by first providing some background regarding SAR studies of nonlinear internal waves and reviewing the physical settings under which the phenomenon takes place. The overall number of wave packets and travel

direction is summarized. The topographic feature where the first internal bore is generated is studied in detail and its surface signature in the SAR image is analyzed. Phase speed calculations are performed assuming forcing by the semidiurnal tide. Estimation of the internal wave amplitude is obtained from the soliton half width, which in turn is derived from the distance between the dark and bright patterns of its surface signature in the SAR image. Based on the local bathymetry, wave phase speed, and mixed-layer thickness, as determined from SAR imagery, an estimation of the density contrast between the upper and lower layers is obtained. A two-dimensional spectrum of the SAR image permits the quantification of the packet wavelength, travel direction, and dispersion effects. The large degree of dispersion seen after the packets propagated farther south is associated to changing stratification conditions, possibly related to the seasonal intrusion of the low-salinity plume of the Yangtze River. Finally, the newly introduced Dnoidal model (APEL, 2003) is used to study the evolution of the internal waves as they propagate away from the coast.

### INTERNAL WAVE DETECTION USING SAR

It is known that tidal flow over steep topography depresses the stratification interface generating an internal bore. The bore starts propagating, and its leading edge becomes steeper through nonlinear effects. With time, frequency, and amplitude, dispersion set in and the leading edge of the bore disintegrates into solitons.

Synthetic Aperture Radar detects the variations in sea surface roughness associated with internal waves. These changes in surface roughness due to convergence and divergence translate into bright and dark patterns in the pixel intensity profile of the SAR image. For depression solitary waves, the bright bands in the SAR signature are in the propagation direction. Solitary waves that elevate rather than depress the interface show dark bands in the propagation direction (LIU *et al.*, 1998).

According to the experiments carried out by RAMIREZ and RENOUD (1998) in a 13-m tank, the ebbing tidal currents are responsible for the formation of internal waves at the shelf break. These waves are observed propagating inshore, over the shelf, and offshore away from the shelf. The internal waves under study offer a remarkable opportunity to confirm that the lee-wave formed by a strong ebbing flow over topography can actually lead to offshore propagating waves. A model by LAMB (1994) illustrates the generating mechanism.

### REGIONAL CHARACTERISTICS

The Yellow Sea has an average depth of 44 m and a maximum depth of about 100 m. In the summer, when the stratification is strongest, the mixed layer shallows to the range of 10 m to 20 m. SAR images acquired during that season show a myriad of internal wave signatures approximately between 33° N to 36° N. The focus area extends from 33°12' N to 34°12' N and from 122°6' W to 125°30' W. The soliton train under study propagates from about 34° N, 122° W to 33°24' N, 124°30' W.

The Radarsat data set parameters were the following:

- Date: August 22, 1998
- Time: 0942:25
- Orbit Number: 14604
- Satellite ID: Radarsat-1
- Processing Site: Alaska SAR Facility
- Size: 57,344 kB
- Beam Mode: ScanSar Wide—500 km × 500 km
- Beam Position: SWB
- Product Type: Geocoded
- Ascending/Descending: Ascending
- Pixel Spacing: 100.00 m
- Northernmost Latitude: 36°8'16.44"
- Southernmost Latitude: 31°3'13.32"
- Westernmost Longitude: 121°13'4.8"
- Easternmost Longitude: 127°2'3.48"

During August, the low salinity plume from the Yangtze river can intrude into this region and cause an increase in vertical stratification (HUR, JACOBS, and TEAGUE, 1999). The Yellow Sea Cold Bottom Water is another water mass that can also intrude into this region as it moves southward (PARK, 1986). Therefore, the trains of internal solitary waves, as they propagate southwest, will not only encounter changes in depth but also are likely to come across changing stratification conditions as well.

### INTERNAL BORE GENERATION AND ASSOCIATED BOTTOM TOPOGRAPHY AS SEEN THROUGH SAR

The possibility to "see" shallow topographic features at the bottom using SAR images is achievable because strong tidal currents flowing over bottom topography cause a modulation in the surface current velocity. This, in turn, causes variations in the spectrum of wind-generated waves, which show up subsequently as intensity modulations in the SAR images (HSU, LIU, and MITNIK, 2001).

The M2+S2 tidal amplitudes at the shelf break, where the internal bore under study is formed, range between 1.5 m to 2 m whereas the tidal currents range between 0.6 m/s and 1.2 m/s. The flooding and ebbing tide flowing over a steep topographic feature depresses the stratification creating an internal bore. Note that the shape of the bore follows, to a certain extent, the shape of the shelf break at which it was generated (Figure 1c). The underwater topography reveals itself through quasistationary patterns of bright and dark pixels bands (looking from west to east). The bore, instead, shows an opposite pattern of intensity that goes from dark to bright. Because the bore is traveling east, it should be depressing the stratification. As mentioned in LIU *et al.* (1998), a disturbance of depression can yield a pattern of bright pixels in the direction of travel. In turn, the shallow underwater bathymetry and the associated tidal flow seem to be introducing a disturbance of elevation in the stratification that gives the exact opposite pattern of convergence–divergence at the sea surface. This translates into opposite patterns of pixel intensity in the SAR image. Further information regarding the theory of radar imaging of internal waves and

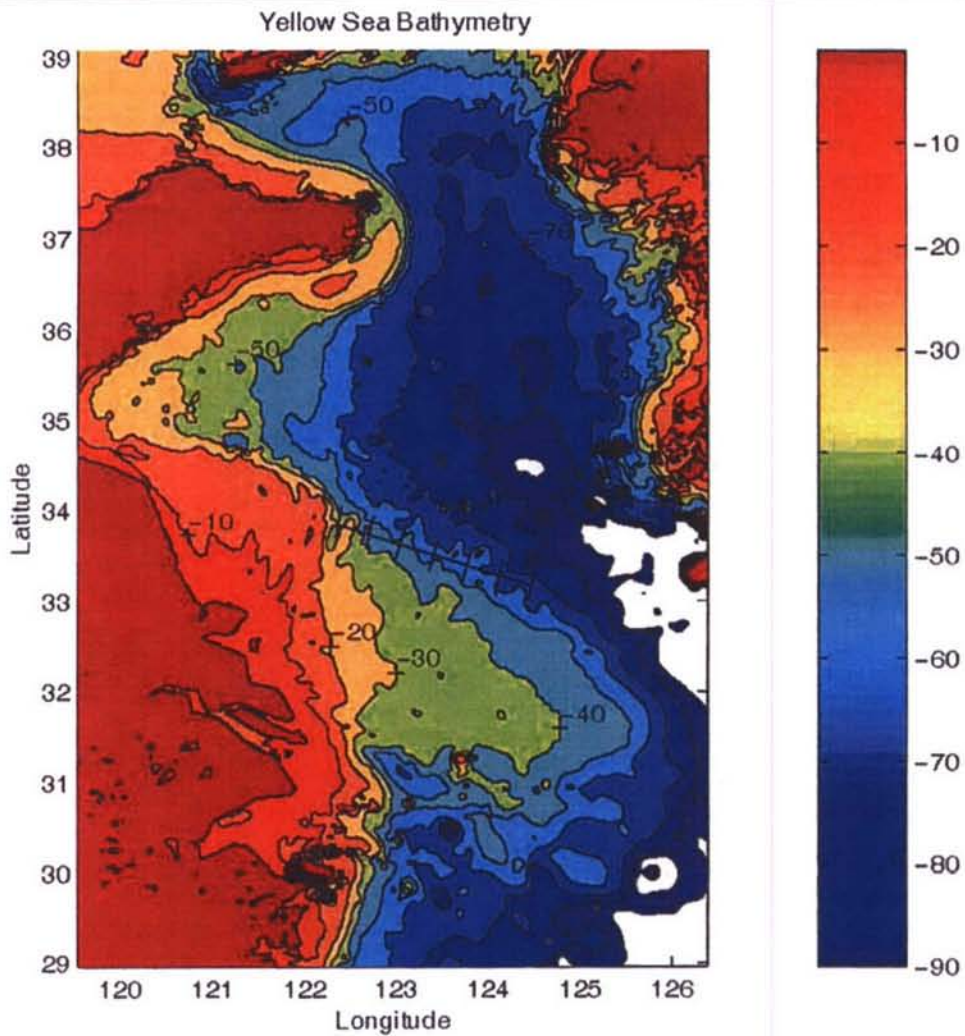


Figure 2. Note the relatively steep slope around 34°N, 122°18' E, just where the internal bore is generated. The bathymetry profile at the site could be related to what appears to be a refraction of the internal bore shortly after its formation. Depth scale is in meters.

surface signature of bottom topography, including their relation to wind and look direction, can be found in ALPERS (1985) and ROMEISER and ALPERS (1997). The appearance of the bathymetry as it is revealed through SAR (Figures 1b and 1d) can be compared with the actual one-minute bathymetry (CHOI, 1999) in Figures 1a and 2. A three-dimensional rendering of this topographic feature was also generated to better understand the phenomenon. The finger-like structure seen in the SAR images is clearly depicted in the topographic variations. A typical depth profile along a transect perpendicular to the shelf break is illustrated in Figure 3.

#### PACKET CHARACTERISTICS AND PARAMETERS

The ScanSAR image shows seven packets of solitary waves propagating 271 km during 3 days along a well-defined direction. The first soliton train extends along its crest for about 132 km. The average distance between packets is 43

km, and the actual location of each packet is summarized in Table 1. The average phase speed is 1.01 m/s. The shape of the packet wave fronts are preserved remarkably well from the second to the fifth tidal period.

An interesting feature of the particular train under study is that after one semidiurnal tidal period the internal bore, which was formed near the shelf break, failed to break up into solitons. Because the original image had a resolution of 100 m/pixel, a full-resolution ScanSAR image with a resolution of 50 m/pixel was analyzed. The mentioned internal bore still did not show any further details at this higher resolution. The fact that the bore appears to fail in breaking up into solitons after one tidal period could be because of the lack of image resolution or it could be the result of the varying underlying bottom topography near the generation point. As a matter of fact, right after the internal bore is formed, it propagates toward a sudden, sill-type topographic feature (Fig-

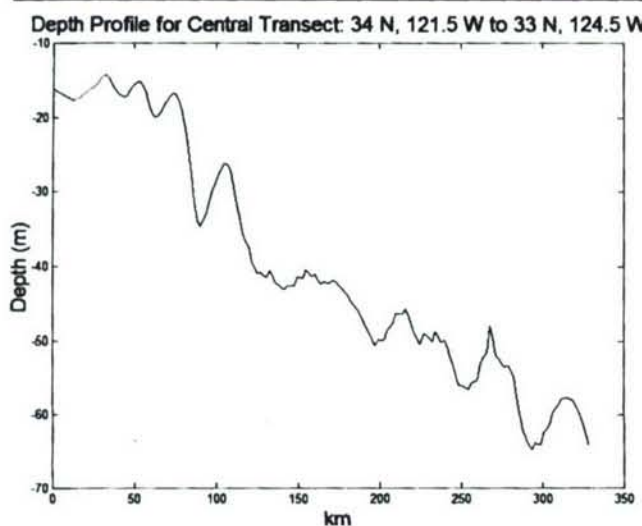


Figure 3. Depth profile follows the central propagation path. After the shelf break, there is a conspicuous underwater feature.

ures 2 and 3), whose interaction with the bore could be the subject of future studies.

Another observation is that the second bore is not parallel to the first. This refraction effect could be related to the northern end of the internal bore propagating over deeper waters than the southern end. The phase speed is between 0.8 m/s and 1.03 m/s depending on what end (south or north) is measured (Figure 4). The third event is also refracted (Table 1) with respect to the second. After this initial refraction, the packets preserve their overall direction for the following four tidal periods. From the first to the second wave packet, there is a clear increase in phase speed. Changes in the shape of the packets could be also because of variations of the vertical stratification along the propagation path, changes of depth, advection by a variable current field, and variations of the tidal forcing from one cycle to the next (PORTER and THOMPSON, 1999).

Along the travel path, there is a depth gradient, from shallow to deep water, not only in the propagation direction but also in the along-crest direction with the southern end of the trains being over shallower waters than their northern ends. This probably accounts for the fact that most wavelengths,

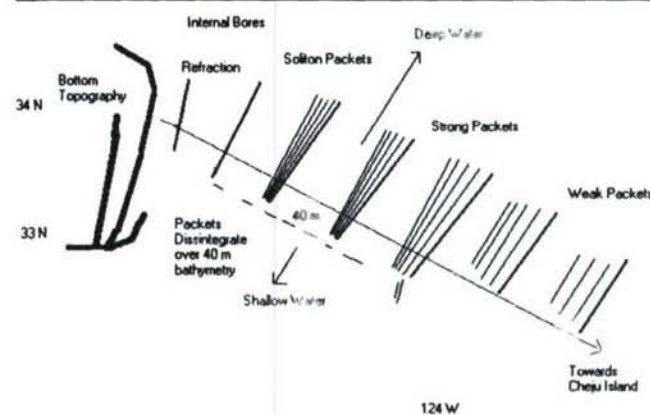


Figure 4. Main characteristics of the internal wave train.

inferred from the SAR image, are smaller toward the south end of the train fronts than toward the north end. In addition, note that as the south end of the wave crest enters shallow waters, its signature disappears. In this article, we will show that the joint consideration of packet's structure, propagation direction, pattern of pixel brightness in the SAR imagery, and extent of dispersion in conjunction with any observed refraction permits us to speculate regarding the overall profile of bottom topography, variable current fields that might be advecting the soliton trains, and spatial density distribution in the region.

#### MEASURING INTERNAL WAVE PARAMETERS FROM SAR IMAGERY

There are four parameters that can be directly measured from SAR images: the packet's phase speed, the soliton half-width, the wavelength at the trailing ends of the packets, and the stretched wavelength. The phase speed can be calculated assuming forcing by the M2 tide (12.42 h) and measuring the distance between the packets fronts. In this particular case study, there is little variation in the phase speed from one packet to the next for the duration of the different tidal periods. This is an indication that the background current speed is fairly constant along the propagation path.

The half-width length scale  $L$  of the solitons can be obtained from the distance that exists between the patterns of

Table 1. Evolution of a packet of internal waves as it propagates during three days in the Yellow Sea.

Soliton Train #	Bore 1	Bore 2 Refracted	Packet 1 Refracted	Packet 2	Packet 3	Packet 4	Packet 5
Time (h)	0	12.4	24.8	37.2	49.6	62	74.4
Distance (km)		36–46	72–93	132	178	226	272
Phase speed: C (m/s)		0.8–1.03	0.8–1.05	1.098	1.03	1.075	1.03
Dominant Wavelengths:							
$\lambda_1$ (m)			530	530	530	530	
$\lambda_2$ (m)			630	670	670	670	
$\lambda_3$ (m)				930	1000	930	
$\lambda_4$ (m)					1200	1200	
$\lambda_5$ (m)					1600	1600	
$\lambda_6$ (m)						2300	2400

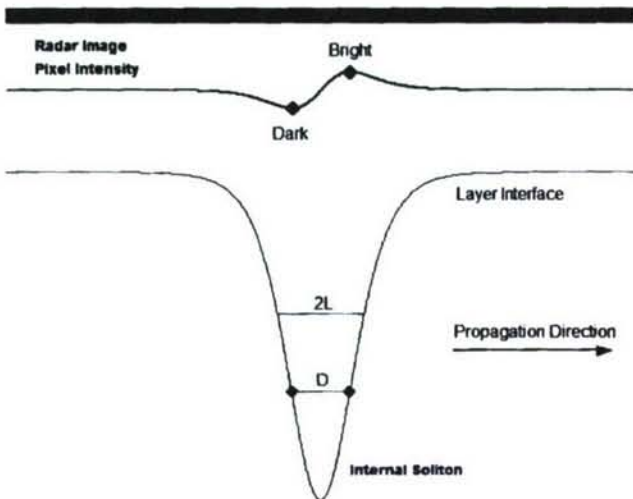


Figure 5. Relation between the isopycnal displacement caused by the internal solitary wave and the pixel intensity pattern in the SAR image. The distance between the dark and bright spots is termed  $D$ . The soliton half-width length scale is termed  $L$ .

bright and dark pixels in the SAR imagery. These pixel arrangements correspond to areas of peak convergence and divergence at the sea surface. Convergence and divergence at the sea surface are related to the surface strain, which is the horizontal gradient of the surface velocity. The analytical functional profile of the surface current, in turn, has the same  $\text{sech}^2$  outline as the isopycnal displacement (see Equations 1 and 2) caused by the internal wave but with opposite phase. The peaks and the troughs in the surface strain give the peak in convergence and divergence and can be found by using the nulls of the first derivative of the strain rate, which is, therefore, the second derivative of the horizontal current. Hence, these points of maximum convergence and divergence correspond to the inflection points of the surface current functional profile. Because this current has the same " $\text{sech}^2$ " shape as the isopycnal displacement, they also correspond to the inflection points in the soliton functional representation. Because the surface strain rate can be considered, on a first-order approximation, roughly proportional to variations in the pixel intensities in the image (LIU et al., 1998), we can define  $D$  as the distance between the inflection points in the soliton profile. This is equivalent to saying that  $D$  is the distance between the bright and dark bands in the pixel intensity patterns of the SAR image. Because the half-width length scale  $L$  of the soliton is a parameter in the argument of its  $\text{sech}^2$  functional profile, it can be easily related to the distance between the inflection points of the curve through differentiation of the analytical solution for the horizontal velocity. The positions of peak divergence and convergence are obtained by setting the second derivative of velocity zero. This relation gives  $L = D/1.32$  (Small et al., 1999). Given our system look direction, Figure 5 depicts the relation between the isopycnal displacement caused by the internal solitary wave and the pixel intensity distribution in the SAR image. Further discussions regarding SAR imaging of internal waves

in association with wind and look direction can be found in ROMEISER and ALPERS (1997). The inflection points in the isopycnal displacement are correlated to the maximum and minimum pixel brightness. Note that  $D$  is larger than  $L$  and that  $2L$  is a good indication of soliton width. In our case study, we estimated  $D$  at 150 m to 200 m, which gives an  $L$  between 113 m and 151 m. We will show later that the soliton half-width can be used in combination with upper and lower layer depth to obtain an estimate of the isopycnal displacement.

The wavelength at the trailing end of the packet,  $\lambda_0$  remains constant as the packets evolve with time and it is related to the isopycnal displacement and to the parameters of dispersion and nonlinearity. The trailing end wavelength was estimated at between 300 m and 350 m. The distance between successive solitons along the packet is termed "stretched wavelength,"  $\lambda$ , and it is dependent on the degree of nonlinearity. The stretched wavelength is always larger than the wavelength at the trailing end of the packet.

## MONITORING THE EFFECTS OF DISPERSION

The leading wave in the packet has the largest amplitude. Because the soliton phase speed is related to its amplitude, the leading wave in the packet travels faster than the rest (PORTER and THOMPSON, 1999). Therefore, the distance between a given wave crest and the next decreases from the front to the back of the packet. Hence, the solitons propagate along the density interface as an internal wave packet with rank-ordered amplitudes and wavelengths.

A two-dimensional Fourier spectrum of a 20-km  $\times$  20-km section of the SAR image was taken for each wave train along central transects. As the second internal bore propagates away from the shelf, it breaks up into solitons where we can see a tightly packed soliton train with a leading wavelength in the order of 530 m to 670 m (Figure 1e). The surface spectra routine gives wavelength in meters and propagation direction with 180° of ambiguity (Figure 6a). The surface spectra corresponding to the packet shown in Figure 1f is depicted in Figure 6b. After several tidal periods, the spectra shows wavelengths ranging from 530 m or less at the trailing end of the packet to 2400 m at the front end (Figures 1g and 6c).

As the packet propagates, the surface spectra clearly shows the effects of dispersion with distance (time). Table 1 summarizes the dominant wavelengths in the packets, as seen in the two-dimensional Fourier spectra vs. distance (time). In general, the leading wavelength measured directly from the SAR image is larger than the largest detected by the two-dimensional spectra. This is because the image is coarse, and sometimes several secondary wavelengths measure about the same, thus, concentrating the most spectral energy at the particular wavelength. In this regard LEVINE and BOYD (1998) noted that, in practice, we can usually find a few solitons within a packet that are not rank ordered.

For the first three events, the effects of refraction were pointed out. For the last four packets, measures were taken along a representative transect close to the center of the propagation path. The wavelengths at the trailing end of the packets tend to remain the same whereas the wavelengths near

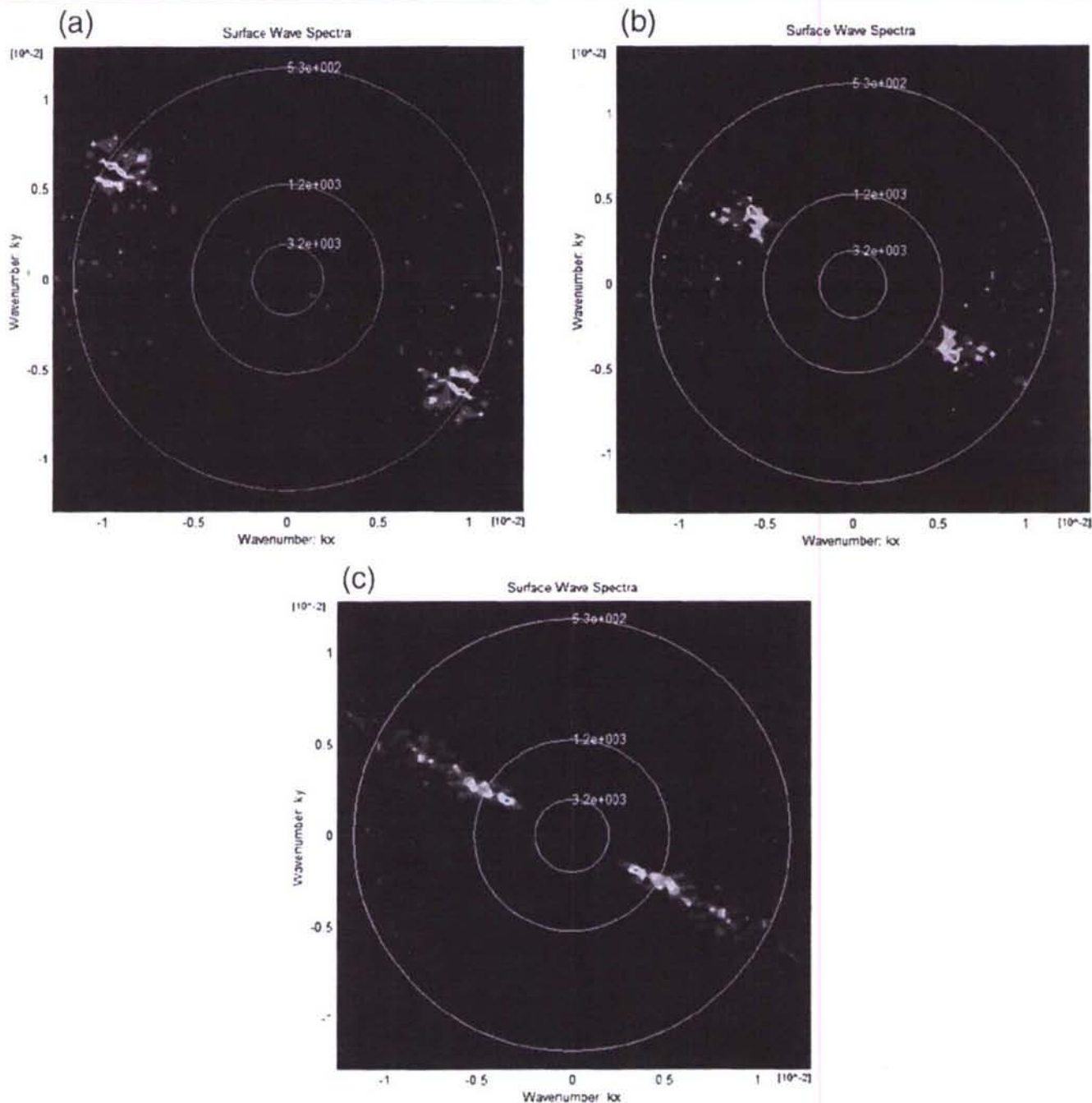


Figure 6. The wavelengths in the first train are tightly packed and show little sign of dispersion. This can be seen in the actual radar imagery (Figure 1e) as well as in the surface wave spectra of the soliton train (a). Wavelength is given, in meters, by the concentric circles. Figures (b) and (c) depict the surface wave spectra showing the effects of dispersion in the packets shown at Figure 1f and Figure 1g.

the leading edge tend to increase. This is because the centroid of the packet travels at the long-wave, linear phase speed  $c_0$ , whereas the front of the packet travels at the nonlinear phase speed  $c$  (APEL, 2003). The nonlinear phase speed is larger than the linear phase speed, and this accounts for the in-

creasingly larger wavelengths observed at the leading edge of the packets.

The amount of dispersion observed in these trains is significant, and because different trains at different times show different degrees of dispersion, it is possible to conclude that

changing conditions in stratification and depth or advection by variable current fields combined with the nonlinear characteristics of the phenomenon could be assisting the extremely large spread in wavelength seen at the front. Note that from the second to the third packet, the wavelengths at the leading end of the packet almost double (Figures 1f and 1g). This is consistent with a suggestion that propagation properties could be sensitive to slight variations in the stratification (LEVINE and BOYD, 1998).

#### ASSESSING WATER COLUMN PROPERTIES BASED ON SAR IMAGES OF INTERNAL WAVES AND A TWO-LAYER MODEL

Given the internal wave characteristics described above, the known bottom topography, and the historical climatological data, changes in vertical stratification along the propagation path could be remotely inferred from the SAR data. These could include variations in the mixed-layer depth as well as changes in the fractional density difference between the layers. Although the stratification in the summer is strong with the mixed layer at a relatively constant depth, as the train of solitary waves travel for 3 days along a 272-km path, they are likely to encounter variable depth and stratification conditions. This particular propagation path is close to the boundary of the Yellow Sea and the northern East China Sea. During the month of August, stratification conditions could vary along this transect due to uneven intrusion of different water masses such as the low-salinity plume from the Yangtze River combined with the Taiwan Warm Current Water (Yangtze River Diluted Water) and the Yellow Sea Cold Bottom Water (PARK, 1986; SU and WENG, 1994).

#### Inference of Mixed Layer Depth Behavior from SAR Imagery

One of the methods reported in the literature (PORTER and THOMPSON, 1999; PORTER *et al.*, 2001) for determining the mixed-layer depth is based on the location, as inferred from SAR observations of the region, where the internal wave signature disappears. This technique is based on different studies (HELFRIECH, 1992; HELFRICH and MELVILLE, 1986; SAFARINIA and KAO, 1996), which show that dissipation of internal waves propagating into shoaling waters occurs when both layers achieve equal widths. Thus, knowledge of the bathymetry at the location where the internal wave signature can no longer be seen allows an estimation of the mixed-layer depth.

Another technique can be inferred from the processes studies reported by LIU *et al.* (1998), in which depression solitons that are propagating into shoaling waters change into solitons of elevation. This phenomenon, where the solitons change from depression to elevation disturbances, occurs after passing a location at which both layers, of a two-layer ocean, are of equal width. After this inversion has occurred, the patterns of surface divergence and convergence at the sea surface also change, and the pixels in the propagation direction become dark rather than bright. SAR observations and numerical simulations of this process can be found in Liu *et al.* (1998).

It is evident, looking at the SAR image (Figures 1b and 1d) in correlation with the underlying bathymetry (Figure 2), that the internal bore has originated along the shelf break starting at depths that are in the range of 30 m to 40 m. The shelf edge surface signature, however, continues south over shallower waters. Because there is no apparent reason for this to happen, other than the existing depth and stratification conditions, we hypothesize that the mixed-layer depth could be near the critical point at this location. This allows a rough estimation, which should be half the depth at which the disturbances are no longer seen, of approximately 20 m. This speculation, which loosely follows the first technique for mixed-layer depth determination, is in very good agreement with historical climatology (NAVOCEANO, 1997) for the region.

It could be argued that the surface signature of an internal wave could also become negligible or nonexistent due to adverse wind conditions and not necessarily because of its disintegration. It is highly unlikely, however, that this sharp cutoff in the surface signature seen in the along-crest direction, throughout all the packets, could be because of the wind. If this were the case, the surface signature of the underwater topography, which is roughly parallel to the trains, should also show a sharp cutoff in that direction.

To apply the second methodology, we need to detect a definitive change in the pattern of pixel brightness along the packet's propagation direction. Although no strong indication of such a phenomenon has been detected in the image under study, there is an internal bore in the proximity of the 40-m isobath that warrants further studies through the use of more sophisticated image-processing techniques.

#### A Simplified Two-Layer Model

Shallow sea internal solitons are usually modeled based on the classical Korteweg-deVries (K-dV) equation:

$$\frac{\partial \eta}{\partial t} + (c_0 + \alpha \eta) \frac{\partial \eta}{\partial x} + \gamma \frac{\partial^3 \eta}{\partial x^3} = 0 \quad (1)$$

where  $\eta$  is the displacement of the isopycnal surface,  $c_0$  is the linear phase speed,  $\alpha$  is the nonlinear coefficient, and  $\gamma$  is the dispersion coefficient. The K-dV equation can be solved for a two-layer model representation of the ocean. The solution consists of an invariant squared hyperbolic secant pulse and a Cnoidal-wave represented by a periodic Cnoidal Jacobian elliptic function (APEL, 2003; GERKEMA, 1994). The single soliton form-preserving solution in the ocean has been represented by the hyperbolic secant pulse (OSBORNE and BURCH, 1980) and is given by Equation (2).

$$\eta(x, t) = -\eta_0 \left[ \operatorname{sech} \left( \frac{x - ct}{L} \right) \right]^2 \quad (2)$$

where  $\eta_0$  is the amplitude or peak pycnocline displacement,  $c$  the phase speed, and  $L$  is the soliton characteristic half-width length scale. Equations (3) to (8) give the coefficients of the K-dV equation for a two-layer model with upper and lower layer widths  $h1$  and  $h2$ , respectively (OSBORNE and BURCH, 1980).

Table 2. Summary of changes in depth, phase speed, amplitude, and density contrast as the internal waves propagate east southeast along a central transect.

$D = 150 \text{ m}$	$L = 113.6 \text{ m}$	$C (\text{m/s})$ from SAR	$h1 (\text{m})$ from SAR	Depth (m) from Bathymetry	$\eta_0 (\text{m})$ from 2-Layer Model	$\Delta\rho_{\text{norm}} (\rho_2 - \rho_1)/\rho_2$ from 2-Layer Model	$\alpha$ from 2-Layer Model	$\gamma$ from 2-Layer Model
Bore 2		0.915	20	50	3.7	0.00669	-0.00221	88.75
Packet 1		0.925	20	50	3.7	0.0068	-0.0224	89.7
Packet 2		1.098	20	60	3.3	0.0085	-0.039	140.59
Packet 3		1.03	20	60	3.3	0.0075	-0.037	131.89
Packet 4		1.075	20	60	3.3	0.0081	-0.0378	137.6
Packet 5		1.03	20	70	3.44	0.0068	-0.044	163.24

$$\eta_0 = \frac{1}{3(h2 - h1)} \left( \frac{2h1h2}{L} \right)^2 \quad (3)$$

$$\Delta\rho_{\text{norm}} = \frac{c^2}{g \frac{h1h2}{h1 + h2} \left[ \frac{\eta_0(h2 - h1)}{2h1h2} + 1 \right]^2} \quad (4)$$

$$c_0 = \sqrt{\left( g \frac{h1h2}{h1 + h2} \Delta\rho_{\text{norm}} \right)} \quad (5)$$

$$\alpha = 3c_0 \frac{h1 - h2}{2h1h2} \quad (6)$$

$$\gamma = \frac{c_0 h1h2}{6}. \quad (7)$$

#### Determination of the Density Contrast between Layers Based on SAR Imagery and the Two-Layer Model Equations

Using the half-width of the solitons, as measured from the SAR image, assuming that the upper layer roughly preserves its width along the propagation path, and considering the bathymetry for the region, we can estimate the density contrast between both layers. Although only historical data are available to validate our results, to establish the usefulness of this technique, the two-layer model equations and observations made from SAR will be used to infer fractional density difference,  $(\rho_2 - \rho_1)/\rho_2$ , between both layers along the propagation path.

The upper layer thickness is  $h1$ , and the lower layer thickness is  $h2$  with associated densities  $\Delta_1$  and  $\Delta_2$ , the density difference is  $\Delta\rho = \rho_2 - \rho_1$ , and the fractional density difference or normalized density is  $\Delta\rho_{\text{norm}} = (\rho_2 - \rho_1)/\rho_2$ . From the knowledge of the phase speed  $c$ , the distance between bright and dark pixels bands in the SAR image  $D$ , and the layer thickness, the equations describing a simplified two-layer model can be used to calculate the density contrast between a two-layer structure.

The phase speed of the solitons can be obtained by assuming that the spacing between the soliton packets is the result of the semidiurnal tidal forcing (12.4 h) and by measuring the distance between the wave fronts. We have done this in a central transect along the propagation path. In the along-crest direction, there is a steep gradient in bathymetry.

Calculations are illustrated for packet number three. The third packet has an estimated phase speed of  $c = 1.03 \text{ m/s}$  along a central transect, the distance between dark and

bright pixels was estimated at  $D = 150 \text{ m}$  from SAR imagery, the bottom,  $h1 + h2$ , was estimated at  $60 \text{ m}$  from the bathymetry, and the mixed-layer depth was estimated at  $h1 = 20 \text{ m}$ , as explained in a previous section. Equations (3) to (7) applied to the third internal wave packet give the following results:

$$L = 113.6 \text{ m}, \quad \eta_0 = 3.3, \quad \Delta\rho_{\text{norm}} = 0.0075, \\ c_0 = 0.989, \quad \alpha = -0.037, \quad \gamma = 131.89. \quad (8)$$

The overall results are summarized in Table 2 for the different depths and phase speeds along the propagation path with the mixed-layer depth assumed to be constant. As the internal waves propagate east southeast, the density contrast tends to increase (Table 2), and because there is no large variations in depth along this transect, the increase could be because of the uneven intrusion of different water masses along the propagation path. This is consistent with the stratification conditions that are known to exist during the month of August when the low-salinity plume of the Yangtze River is farthest north (HUR, JACOBS, and TEAGUE, 1999).

Note that from the second to the third packet, the leading wavelengths almost double (Figures 1f and 1g). This could be a manifestation of the highly nonlinear characteristics of this phenomenon coupled to changing stratification conditions. An increase in the density contrast should cause an increase in the nonlinear phase speed at the leading end of the packet, and as a consequence, the increase in wavelength at the front could be larger than that expected under unchanged stratification conditions. Other packets arriving to the area from different points also show a similar large degree of dispersion, thus supporting the hypothesis that there could be an intrusion of lighter water into the region.

From carefully measured phase speed and depth distributions at various points along the internal wave train, a two-dimensional density contrast field of the area could be constructed. When the lower layer density is known from historical climatology, then the upper layer density can also be estimated. The lower layer is usually more stable, and its density does not change as much as it does in the upper layer. Even though the absolute values of the estimates for the density contrast in Table 2 appear high, it is likely that from a comparative point of view, from one region to another, or from within the same area but at different times, they could provide useful information regarding the regional, upper layer, relative density distribution.

The internal wave train under study propagates for 270 km

and measures up to 130 km in the along-crest direction, indicating an area of about 35,100 km<sup>2</sup>, at the entrance of the Yellow Sea, which could be remotely monitored. Note, however, that the existence of this particular internal wave train could be seasonal and only peak spring tides might support its formation. The study of further SAR imagery from this area is needed to clarify this point and to monitor whether the dispersion extent observed throughout the internal wave packets is related to seasonal changes in stratification conditions, variable current fields, or other regional phenomena. Although some of these conclusions are speculative, they serve to illustrate the potential of this methodology. Coastal ocean monitoring, including the capability to identify and interpret surface features, can be further enhanced when SAR imagery is used in combination with optical and infrared sensors (JOHANNESSEN, 2000).

### THE DNOIDAL MODEL

The recently introduced analytical Dnoidal model (APEL, 2003) predicts the most important characteristics of continental shelf solitons as they evolve in time and space. The model is based on a solution of the K-dV equation for the amplitude and the Taylor-Goldstein equation for the vertical structure. Among the properties that can be monitored with this model, we have the number of solitons, linear wave speed, waveform, and attenuation. Synthetic Aperture Radar images, which provide the means to measure important internal wave parameters, such as wavelength and half-width, can be used in conjunction with historical climatological data and numerical or analytical models to further our understanding of the dynamics of solitons in the ocean.

### Model Background

The solution to Equation (1) given by the hyperbolic secant profile in Equation (2) does not allow the addition of new solitons pulses as the packet propagates, does not provide for the dispersion effects as soliton trains evolve with time, and does not model the depression of the isopycnal displacement by the internal tide. APEL (2003) used a little-known solution to Equation (1) to model the mentioned effects. GUREVICH and PTTAEVSKII (1973) originally used this solution to describe collisionless shock waves in plasma. This solution, termed the Dnoidal solution, is multiplied by an *ad hoc* term that models the recovery of the isopycnal surface to its equilibrium state. It is also an asymptotic solution to the K-dV equation and, therefore, not valid near the internal wave origination point (APEL, 2003). As time passes the model adds one oscillation per buoyancy period. According to the model, the displacement,  $\eta(x, z, t; k)$  of an isopycnal surface from equilibrium can be written as in Equation (9):

$$\eta(x, z, t; k) = \sum_n \eta_{0n} W_{k,n}(z) I(x, t) e^{-az(x-x_0)} \times \left\{ 2dn_s^2(x) \left[ \frac{1}{2} k_0 (x - V_n t) \right] - [1 - s^2(x)] \right\}. \quad (9)$$

The function  $dn_s(x)$  is one of the Jacobian elliptic functions (PRESS *et al.*, 1992), which in analogy to the well-known oscillatory K-dV solution named "Cnoidal" was termed "Dnoidal" by APEL (2003). The function  $W_{k,n}(z)$ , which gives the vertical structure (Appendix A), is an eigenfunction of the Taylor-Goldstein equation with eigenvalue  $k = 2\pi/\lambda_0$ . The wave number  $k_0$  is related to the wavelength at the trailing edge of the packet,  $\lambda_0$ , as  $k_0 = 2\pi/\lambda_0$ .  $I(x, t)$  is the recovery function that models the return to equilibrium over the semi-diurnal tidal cycle.  $V$  is the nonlinear phase velocity. The nonlinear parameter,  $s$ , modulates the amplitude and the wavelength, thus, defining the limits of the packet. The internal vertical modes of the water column are denoted by  $n$ . The exponential factor is an attenuation function used to reduce the amplitudes. The values of  $a$  and  $x_0$  are empirically determined. Appendix A provides additional details regarding the model.

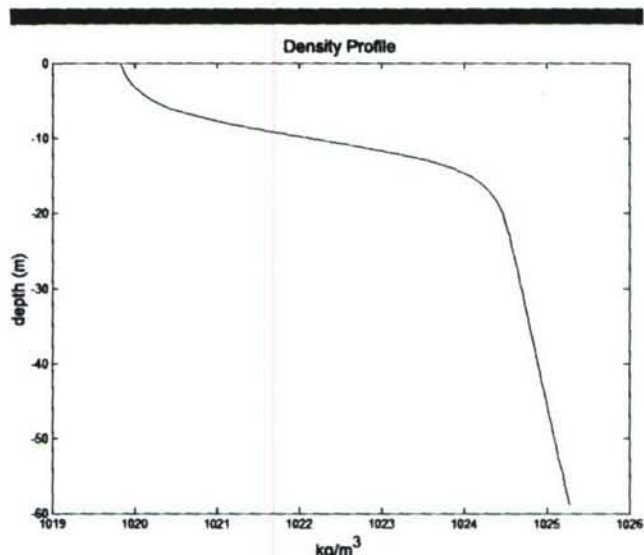


Figure 7. Typical density profile for the region under study.

In summary, the Dnoidal model reproduces the sharp onset seen at the front of the packet and, as the wave packet proceeds in space and time, increases packet length and wavelength while developing additional oscillations. It also models the long-term depression seen at the trailing end of the packets. A study of the dynamics of the internal solitons near Gibraltar using the Dnoidal model and SAR data can be found in APEL and WORCESTER (2000). A comprehensive description of this new analytical model is given in APEL (2003).

### Model Initialization Using Climatological and SAR Data

Because the model is based on a solution to the K-dV equation for the amplitude and the Taylor-Goldstein equation for the vertical structure, it is divided in two distinct parts. The model is structured so that the first module corresponds to the Taylor-Goldstein equation, which gives the vertical structure (Appendix A). The results from this part are then used as input to a second module for the "Dnoidal" calculations, which give the simulation final results. In addition to density and current profiles, the computations of the first module re-

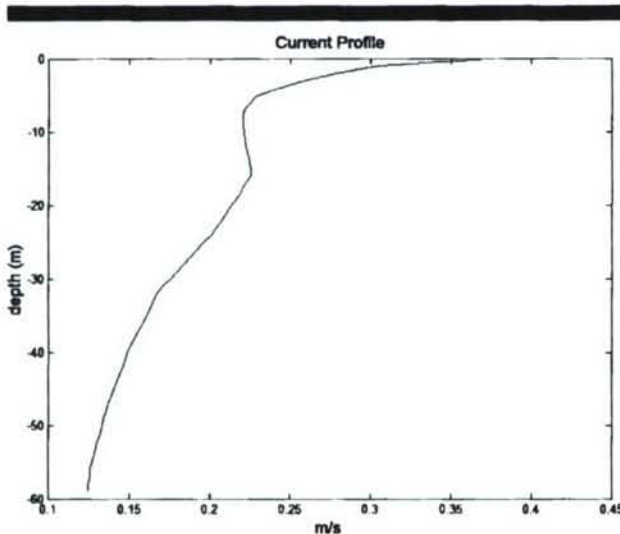


Figure 8. Typical current profile for the region under study.

quire an estimation of the wavelength at the trailing edge of the packet,  $\lambda_0$ . The wavelength at the trailing end of the packets can be measured from SAR images and the wave number  $k_0$  can then be calculated as  $k_0 = 2\pi/\lambda_0$ . The wave number, in turn, is related to the amplitude,  $\eta_0$ , to the nonlinear coefficient,  $\alpha$ , and to the dispersion coefficient,  $\gamma$ , by the following equation:

$$\frac{1}{2}k_0 = \left( \frac{-\alpha\eta_0}{6\gamma} \right)^{1/2} \quad (10)$$

This expression can be used to establish consistency between the value of  $k_0$  and  $\eta_0$  obtained from SAR imagery and the parameter values  $\alpha$  and  $\gamma$  given by the first section of the model.

The first module provides the first-mode eigenfunction from the Taylor-Goldstein equation, which gives the vertical structure function, the parameter of nonlinearity  $\alpha$ , the parameter of dispersion  $\gamma$ , and the linear phase speed, among others. The second module in the model uses the output of the first section to carry out the Dnoidal calculations. It also requires an estimation of the amplitude of the leading soliton pulse. This estimate can be obtained, using a two-layer model, from the half-width of the soliton and the upper and lower layer widths in Equation (3). The half-width of the soliton, as explained before, is another parameter that can be extracted from SAR imagery.

According to numerical evaluations, the value of  $\alpha\eta_0$  controls the number of oscillations and can be tuned to provide the correct number of solitons in the packet. In general the parameter  $\alpha$  used for the Dnoidal calculations has to be taken smaller than the one calculated by the model's first module. This could be because during strong pycnocline displacements the effective depth of the upper layer ( $h_1$ ) becomes larger, thus decreasing  $\alpha$  and increasing  $\gamma$ , in Equations (6) and (7). APEL (2003) suggests that a more precise estimate of  $\alpha$  may be inferred considering a pycnocline depth that, as the wave

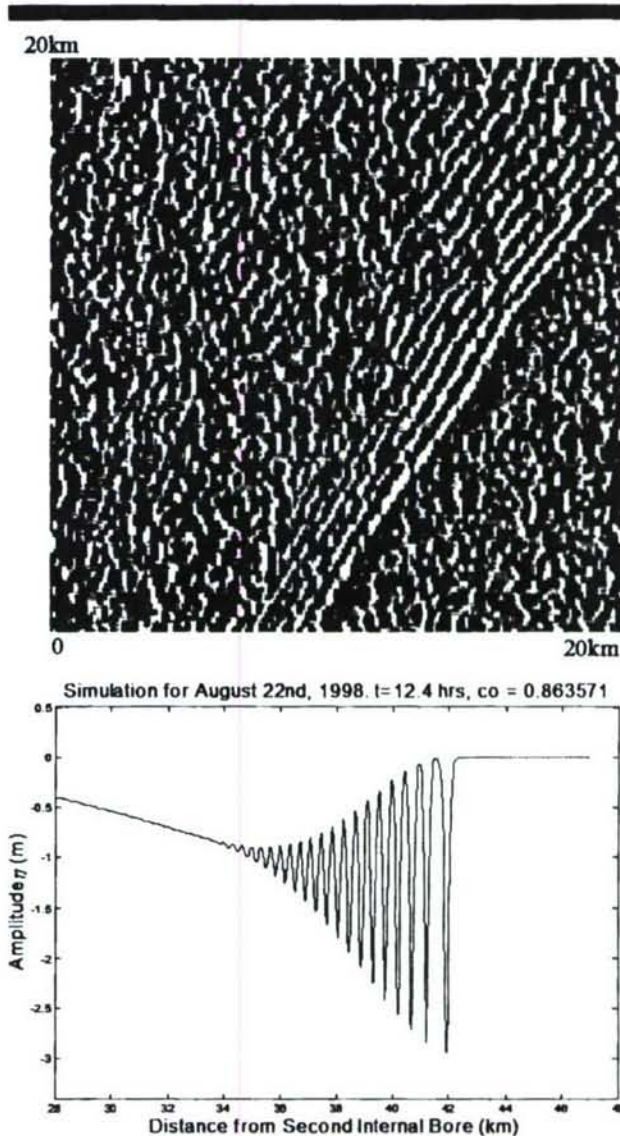


Figure 9. Simulation results vs. observed internal wave packet after one tidal period. The area covered is about 20 km  $\times$  20 km and can be located in Figure 1e.

passes, is displaced by  $2\eta_0$ , rather than assuming the equilibrium depth ( $h_1$ ).

In this simulation, typical density and current profiles for the region were used to initialize the model (Figures 7 and 8). The trailing edge wavelength was estimated at  $\lambda_0 = 320$  m, the half-width of the leading soliton pulse was estimated from SAR imagery at  $L = 113.6$  m, and the amplitude was calculated in a preceding section using Equation (3), which gave  $\eta_0 = 3.3$  m. The total depth was assumed at 60 m, and the upper layer depth was estimated at 20 m according to previous discussions. The calculations from the first module in the model gave  $\alpha = -0.1072$ , a rather high estimate, and  $\gamma = 83.9817$ . The value of  $\alpha$  was modified to  $\alpha = -0.0397$  to

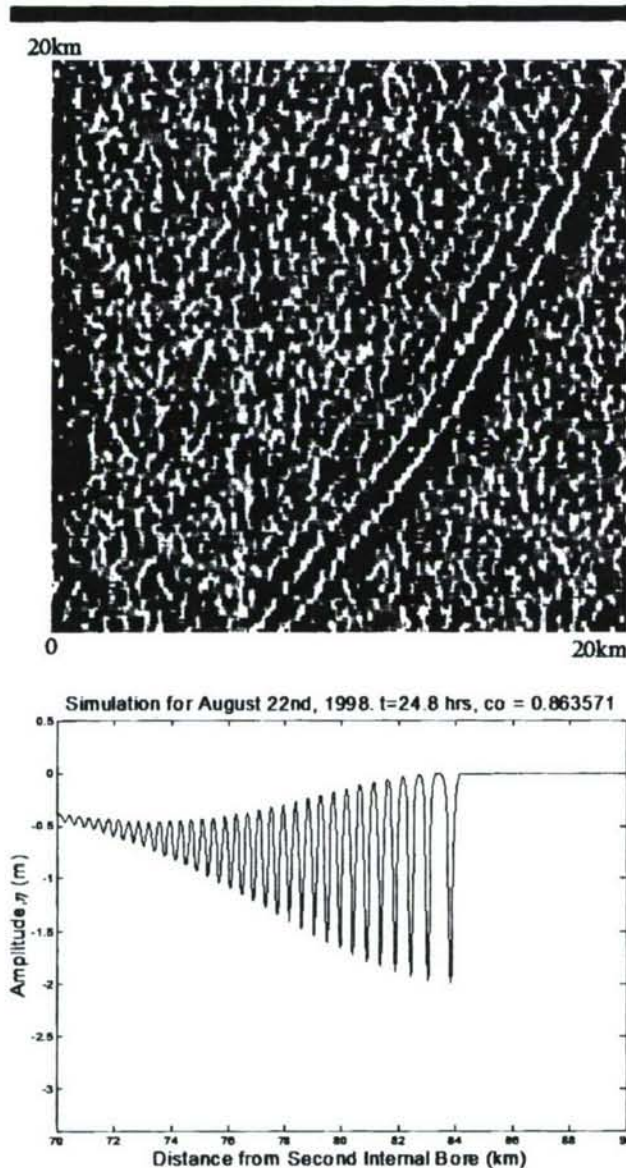


Figure 10. Simulation results versus observed internal wave packet after two tidal periods. The area covered is about 20 km × 20 km and can be located in Figure 1f.

achieve consistency within the relation given by Equation (10). For these values, the right side of Equation (10) gives 0.0098 whereas the left side gives 0.0161, which are in fairly good agreement. The selected value for  $\alpha$  in combination with  $\eta_0 = 3.3$  m provides a number of oscillations in harmony with those shown in SAR imagery for the first two tidal periods (Figures 9 and 10). The linear phase speed was determined by the first calculations in the model at  $c_0 = 0.8636$ . Model results were monitored for three tidal periods after the initial bore broke up into solitons.

#### Validation Studies Using SAR Imagery

The model was initialized as described in the previous section and run for the first tidal period (12.4 h). Results are depicted in Figure 9, where they are compared with SAR imagery for the first soliton packet. The area covered is 20 km × 20 km and can also be seen in Figure 1e. There is consistency between observations and model results in terms of the leading wavelength, number of solitons, and distance traveled by the packet. The number of solitons seen in the SAR image when looking at the upper part of the picture is roughly the same as the number predicted by the model output. Note that there are usually more oscillations in a simulated packet than the one appearing in the SAR image. This is because of SAR resolution problems and less than perfect conditions for image acquisition.

For the second tidal period (24.8 h), we found a similar agreement between the model output and the observed soliton train (Figure 10). In this case the SAR image only shows solitons near the leading edge and near the trailing edge of the soliton train. This could be because of wind conditions in the area that are partially masking the surface manifestation of the internal waves. Note that the surface signature of the internal waves is related to the strain rate and, thus, shifted with respect to the internal wave amplitude displacements. Table 3 compares the main packet characteristics as observed from SAR with the actual model results.

The slight mismatch in amplitude between model results and observations arises because the model was initialized with a 60 m depth and with an amplitude of 3.3 m, which was the one given by the two-layer model equations. After 12.4 h, the Dnoidal model shows that the amplitude has decreased to 3 m. In practice, the first train is more than 50 m in depth with an amplitude of 3.7 m whereas the second train is more than 60 m in depth with an amplitude of 3.3 m.

Figure 11 shows the evolution of the soliton train, as de-

Table 3. Main packet characteristics as observed from SAR compared with model results.

	Packet Parameters	Observations from SAR	Dnoidal Model
First packet (12.4 h)	Number of solitons	13 to 15	20
	Distance from 2nd bore	41.5 km	42 km
	Leading wavelength	670 m	700 m
	Peak pycnocline Displacement	3.7 m (two-layer model)	3 m
Second Packet (24.8 hrs)	Number of solitons	15 to 20	30
	Distance from 2nd bore	91 km	84 km
	Leading wavelength	1000 m	801 m
	Peak pycnocline Displacement	3.3 m (two-layer model)	2 m

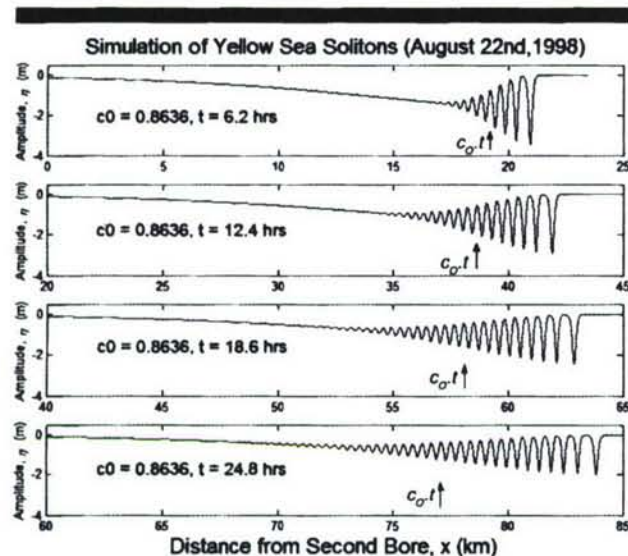


Figure 11. Soliton evolution modeled for two tidal periods. The arrows correspond to the centroid of the packet  $c_0 t$  which moves with the linear phase speed  $c_0$ . The front of the packet moves with the nonlinear phase speed  $c$ .

determined by the Dnoidal model, at intervals of 6.2 h and during two tidal periods. The centroid of the packet moves with linear phase speed  $c_0 = 0.8636$ , whereas the front of the packet moves with the nonlinear phase speed  $c$  (APEL, 2003). This causes dispersion, something that is readily seen in Figure 11.

By the third tidal period, the observed internal wave packet shows a very large degree of dispersion (Figure 1g), which the model does not follow. As was mentioned, we suspect that intrusion of lighter water from the plume of the Yangtze River and/or advection by strong, variable current fields coupled with the highly nonlinear characteristics of this phenomenon could be responsible for the large increase in wavelength seen in these images. An adaptation of the model that takes into consideration higher nonlinearities in the K-dV equation as well as changing stratification conditions along the propagation path might be needed to describe these extreme cases of dispersion.

## CONCLUSIONS

An internal wave train that propagated for three days in the Yellow Sea has been analyzed. Because part of the underwater topography was visible through its sea surface manifestation in the SAR imagery, it provided the opportunity to determine with a very good degree of accuracy the origination point of the internal wave train. The depth profile seen at the internal bore origination region was used to initialize a numerical model for investigative studies. Several parameters of the solitary internal waves were derived from the SAR data and used in conjunction with a two-layer model and the Dnoidal model to characterize the dynamics of the solitons as well as to infer some properties of the water column. The

model showed good agreement with observations in the SAR imagery for two tidal periods. There was consistency in terms of number of solitons in the packet, distance traveled by the packet, and to certain extent, in the amount of pycnocline displacement. By the third tidal period, the internal wave packet shows a very large degree of dispersion, which the model does not follow. An adaptation of the model that takes into consideration the higher nonlinearities in the K-dV equation as well as changing stratification conditions and ocean currents along the propagation path might be needed to describe these extreme cases of dispersion. The large degree of dispersion observed within the internal wave packets as they propagated further southeast was postulated to be a possible consequence of an increase in the density contrast due to the seasonal intrusion of the Yangtze River plume into the region. Following this hypothesis, it is clear that sustained observations of internal wave packets in the area could be used to remotely monitor regional and seasonal changes in the upper layer relative density distribution. The study of further SAR imagery is needed to examine whether the dispersion extent seen in these packets of solitary waves is associated with seasonal changes in stratification conditions or with advection by variable current fields along the propagation path.

## ACKNOWLEDGMENTS

We were saddened by the death of our colleague and co-author John Apel during the evolution of this work. He brought valuable experience and physical insight into the article. The SAR images used in this work were obtained from the NASA, Alaska SAR Facility. Our thanks to Shelley Riedlinger for contributing the Yellow Sea mean current profile and advice on tides and currents and to Chris Jackson for pointing out several references and making helpful observations. We are thankful for the detailed list of remarks and corrections made by the reviewers of this article.

## LITERATURE CITED

- ALPERS, W., 1985. Theory of radar imaging of internal waves. *Nature*, Letter to the editor, 314(6008), 245–247.
- APEL, J.R., 2003. A new analytical model for internal solitons in the ocean. *Journal of Physical Oceanography*, 33(11), 2247–2269.
- APEL, J.R. and WORCESTER, P.F., 2000. Internal solitons near Gibraltar: A longitudinal study using ERS-1 & 2 SAR imagery. ESA ERS-ENVISAT Symposium "Looking down to Earth in the New Millennium" (Gothenburg, Sweden), ESA paper SP461.
- CHOI, B.-H., 1999. Digital Atlas for Neighboring Seas of the Korean Peninsula. Laboratory for Coastal and Ocean Dynamics Studies, Sung Kyun Kwan University. Available on compact disk, email: bchoi@yurim.skku.ac.kr.
- GERKEMA, T., 1994. Nonlinear Dispersive Internal Tides: Generation Models for Rotating Ocean. Texel, The Netherlands: Royal Netherlands Institute for Sea Research, doctoral thesis, 149p.
- GUREVICH, A.V. and PITAEVSKII, L.P., 1973. Nonstationary structure of a collisionless shock wave. *Soviet Physics JETP* (ZhETF), 65(3), 590–595.
- HELFRICH, K.R., 1992. Internal solitary wave breaking and run-up on uniform slope. *Journal of Fluid Mechanics*, 243, 133–140.
- HELFRICH, K.R. and MELVILLE, W.K., 1986. On long nonlinear internal waves over slope-shelf topography. *Journal of Fluid Mechanics*, 167, 285–308.
- HSU, M.K., LIU, A.K., and MITNIK, L.M., 2001. Study bottom topography in the Taiwan area with ERS SAR. The 11th Annual Meeting of the PAMS/JECSS (Cheju, Korea), pp. 479–482.

- HUR, H.B.; JACOBS, G.A., and TEAGUE, W.J., 1999. Monthly variations of water masses in the Yellow and East China Seas. *Journal of Oceanography*, 55(2), 171–184.
- JOHANNESSEN, J.A., 2000. Coastal observing systems: the role of synthetic aperture radar. *John Hopkins APL Technical Digest*, 21(1), 41–48.
- LAMB, K.G., 1994. Numerical experiments of internal wave generation by strong tidal flow across a finite amplitude bank edge. *Journal of Geophysical Research*, 99(C1), 843–864.
- LEVINE, M. and BOYD, T., 1998. Nonlinear internal wave observations on the continental shelf. In: DUDA, T.F. and FARMER, D.M. (eds.), *The 1998 WHOI/IOS/ONR Internal Solitary Wave Workshop: Contributed Papers*. Technical Report WHOI-99-07. Woods Hole, MA: Woods Hole Oceanographic Institution, pp. 101–106.
- LIU, A.K.; CHANG, Y.S.; HSU, M.K., and LIANG, N.K., 1998. Evolution of nonlinear internal waves in the East and South China Seas. *Journal of Geophysical Research*, 103(C4), 7995–8008.
- [NAVOCEANO] NAVAL OCEANOGRAPHIC OFFICE, 1997. Data Base Description for Digital Bathymetric Data Base-Variable Resolution (DBDB-V), Version 1.0. Internal report. Stennis Space Center, MS: Naval Oceanographic Office.
- OSBORNE, A.R. and BURCH, T.L., 1980. Internal solitons in the Andaman Sea. *Science*, 208(4443), 451–460.
- PARK, Y.H., 1986. Water characteristics and movements of the Yellow Sea Warm Current in summer. *Journal of Progress in Oceanography*, 17, 243–254.
- PORTER, D.L. and THOMPSON, D.R., 1999. Continental shelf parameters inferred from SAR internal wave observations. *Journal of Atmospheric and Oceanic Technology*, 16, 475–487.
- PORTER, D.L.; THOMPSON, D.R.; ALPERS, W., and ROMEISER, R., 2001. Remotely sensed ocean observations of the coastal mixing and optics site from synthetic aperture radars and advanced very high resolution radiometers. *Journal of Geophysical Research*, 106(C5), 9623–9638.
- PRESS, W.H.; TEUKOLSKY, S.A.; VETTERLING, W.T., and FLANNERY, B.P., 1992. *Numerical Recipes in C*. 2nd edition, Cambridge: Cambridge University Press, pp. 269.
- RAMIREZ, C. and RENOUARD, D., 1998. Generation of internal waves over a shelf. *Dynamic of Atmospheres and Oceans*, 28(1998), 107–125.
- ROMEISER, R. and ALPERS, W., 1997. An improved composite surface model for the radar backscattering cross section of the ocean surface, part 2: model response to surface roughness variations and the radar imaging of underwater bottom topography. *Journal of Geophysical Research*, 102(C11), 25251–25267.
- SAFFARINIA, K., and KAO, T.W., 1996. A numerical study of the breaking of an internal soliton and its interaction with a slope. *Dynamics of Atmosphere and Oceans*, 23(1996), 379–389.
- SMALL, J.; HALLOCK, Z.; PAVEY, G., and SCOTT, J., 1999. Observations of large amplitude internal waves at the Malin Shelf edge during SESAME 1995. *Continental Shelf Research*, 19(1999), 1389–1436.
- SU, Y. and WENG, X., 1994. Water masses in China Seas. In: ZHOU, D.; LIANG, Y-B., and ZENG, C-K. (eds.). *Oceanology of the China Seas*, Volume 1, Boston: Kluwer Academic Publishers, pp. 3–16.
- WARN-VARNAS, A.; CHIN-BING, S.; HAWKINGS, J.; LAMB, K., and TEIXEIRA, M., 2005. Yellow Sea ocean-acoustic solitary wave modeling studies. *Journal of Geophysical Research*, 110, C08001, doi: 10.1029/2004JC002801.

## APPENDIX A

### Dnoidal Model Equations

The Dnoidal model is based on a solution to the K-dV equation for the amplitude and the Taylor-Goldstein equation for the vertical structure. According to APEL (2003), the displacement,  $\eta(x, z, t; k)$  of an isopycnal surface from equilibrium can be written in its final form as in the following equation:

$$\eta(x, z, t; k) = \sum_n \eta_{0n} W_{k,n}(z) I(x, t) e^{-a(x-x_0)} \\ \times \left\{ 2dn_s^2(x) \left[ \frac{1}{2} k_0(x - V_n t) \right] - [1 - s^2(x)] \right\} \quad (\text{A-1})$$

where:

- $d n_s(x)$  Is one of the Jacobian elliptic functions, which depend on the nonlinear parameter  $s$ ;
- $k$  Is an eigenvalue of the Taylor-Goldstein equation:  $k = 2\pi/\lambda$ ;
- $k_0$  Is the wave number and is related to the wavelength at the trailing edge of the packet  $\lambda_0$  as  $k_0 = 2\pi/\lambda_0$ ;
- $n$  Are the internal vertical modes of the water column;
- $\eta_{0n}$  Are the amplitudes of each normal mode;
- $V$  Is the nonlinear phase velocity, which can be written as:

$$V = c_0 \left( 1 + \frac{1 + s^2}{3} \alpha \eta_0 \right) \quad (\text{A-2})$$

- $s$  Is the nonlinear parameter ( $0 < s^2 < 1$ ) that modulates the amplitude and the wavelength thus defining the limits of the packet;
- $e^{-a(x-x_0)}$  Is an attenuation function used to reduce the amplitudes;
- $a$  Is empirically determined:  $a = 2 \times 10^{-2} \text{ km}^{-1}$ ;
- $x_0$  Is empirically determined:  $x_0 = 1 \text{ km}$ ;
- $I(x, t)$  Is the recovery function that models the return to equilibrium over the semidiurnal tidal cycle:

$$I(x, t) = \frac{1}{2} \left[ 1 + \tanh \left( \frac{x - c_0 t - \chi}{L} \right) \right] \quad (\text{A-3})$$

where:

- $L$  Gives a scale;
- $\chi$  Gives a phase to the return to equilibrium profile at the trailing end of the packets; and
- $W_{k,n}(z)$  Gives the vertical structure and is an eigenfunction of the Taylor-Goldstein equation.

### The Vertical Structure Function

The full Taylor-Goldstein equation for linear internal waves governs the vertical structure. If the equation is generalized to consider a streaming velocity  $U_0(z)$ , then for the eigenfunction  $W_{k,n}(z)$  the equation becomes that shown in A-4:

$$\left\{ \frac{d^2}{dz^2} + k^2 \left[ \frac{N^2(z)}{(\omega_n - k \cdot U_0(z))^2} + \frac{d^2 U_0 / dz^2}{k[\omega_n - k \cdot U_0(z)]} - 1 \right] \right\} W_{k,n}(z) = 0 \quad (\text{A-4})$$

The TG equation could be modified to include effects of the Earth's rotation. The resultant equation is more complicated and the solutions are altered but mainly at very low frequencies (APEL, 2003).

Vertical variations in the horizontal mean current velocity  $U_0(z)$  and in the buoyancy frequency  $N(z)$  are allowed. For mode  $n$ , the wave frequency eigenvalue is  $\omega_n$ . After imposing rigid-lid boundary conditions at the surface ( $z = 0$ ) and at the bottom ( $z = -H$ ) this becomes a second-order Sturm-Liouville system (APEL, 2003).